Representing natural climate variability in an event attribution context: Indo-Pakistani heatwave of 2022

Shruti Nath [a,b,*], Mathias Hauser [b], Dominik L. Schumacher [b], Quentin Lejeune [a], Lukas Gudmundsson [b], Yann Quilcaille [b], Pierre Candela [c], Fahad Saeed [a], Sonia I. Seneviratne [b], Carl-Friedrich Schleussner [a,d]

[a] *Climate Analytics, Berlin, Germany*
[b] *Institute of Atmospheric and Climate Science, Department of Environmental Systems Science, ETH Zürich, Switzerland*
[c] *L'Ecole Polytechnique, Paris, France*
[d] *IRI THESys and Geography Faculty, Berlin, Germany*

ARTICLE INFO

ABSTRACT

Attribution of extreme climate events to global climate change as a result of anthropogenic greenhouse gas emissions has become increasingly important. Extreme climate events arise at the intersection of natural climate variability and a forced response of the Earth system to anthropogenic greenhouse gas emissions, which may alter the frequency and severity of such events. Accounting for the effects of both natural climate variability and the forced response to anthropogenic climate change is thus central for the attribution. Here, we investigate the reproducibility of probabilistic extreme event attribution results under more explicit representations of natural climate variability. We employ well-established methodologies deployed in statistical Earth System Model emulators to represent natural climate variability as informed from its spatio-temporal covariance structures. Two approaches towards representing natural climate variability are investigated: (1) where natural climate variability is treated as a single component; and (2) where natural climate variability is disentangled into its annual and seasonal components. We showcase our approaches by attributing the 2022 Indo-Pakistani heatwave to human-induced climate change. We find that explicit representation of annual and seasonal natural climate variability increases the overall uncertainty in attribution results considerably compared to established approaches such as the World Weather Attribution Initiative. The increase in likelihood of such an event occurring as a result of global warming differs slightly between the approaches, mainly due to different assessments of the pre-industrial return periods. Our approach that explicitly resolves annual and seasonal natural climate variability indicates a median increase in likelihood by a factor of 41 (95% range: 6-603). We find a robust signal of increased likelihood and intensification of the event with increasing global warming levels across all approaches. Compared to its present likelihood, under 1.5 °C (2 °C) of global near-surface air temperature increase relative to pre-industrial temperatures, the likelihood of the event would be between 2.2 to 2.5 times (8 to 9 times) higher. We note that regardless of the different statistical approaches to represent natural variability, the outcomes on the conducted event attribution are similar, with minor differences mainly in the uncertainty ranges. Possible reasons for differences are evaluated, including limitations of the proposed approach for this type of application, as well as the specific aspects in which it can provide complementary information to established approaches.

1. Introduction

With the emergence of increasingly severe, and even unprecedented extreme weather events, the science of event attribution has received ever more attention (Otto et al., 2015; Van Oldenborgh et al., 2018; Philip et al., 2020). Among the different methods, probabilistic extreme event attribution — such as developed by the World Weather Attribution Initiative (WWA) (Philip et al., 2020) — has been used for rapid, real-time assessment and attribution of extreme events (Philip et al., 2021; Kimutai et al., 2022). This represents an important step towards swiftly informing the public on the link between extreme events and the warming climate, using well-grounded scientific methods.

A central element of event attribution is the uncertainty in the assessment of natural climate variability (Otto et al., 2012; Stott et al., 2016). This study seeks to demonstrate the reproducibility of probabilistic extreme event attribution results under more explicit representations of natural climate variability. Consistent with existing probabilistic event attribution methods, we employ a statistical framework, but represent natural climate variability by considering the spatiotemporal patterns existing on annual to seasonal scales. To this extent, we consider natural climate variability as composed of short-term spatially correlated processes and statistically represent them by adapting the framework of the Earth System Model (ESM) emulator MESMER (Beusch et al., 2020). MESMER has been designed such that its output mimics the properties of ESM initial-condition ensembles. It does so by combining pattern scaling estimates of the local forced responses of yearly temperatures to Global Mean Temperatures (GMT) – which serve as a proxy to anthropogenic greenhouse gases (GHG) forcings – with stochastically modelled estimates of natural climate variability that conserve spatio-temporal covariance structures (Tebaldi and Arblaster, 2014; Beusch et al., 2020). More recently, MESMER was also extended with a monthly downscaling module, MESMER-M, which models monthly mean temperature and accounts for their skewness and heteroskedasticity (Nath et al., 2022). Here we adapt both MESMER and MESMER-M to allow the emulator to be used for extreme event attribution. This is the first of an emulator based approach for probabilistic event attribution, although previous use cases of emulators in detection and attribution already exist. For example, Beusch et al. (2022) where able to use MESMER coupled to the global emulator MAGICC (Meinshausen et al., 2011) to explore the contributions of major emitters to regional warming, while Watson-parris and Smith (2022) used the global emulator FAIR (Smith et al., 2017) to identify the role of aerosol forcing uncertainty in future warming uncertainty.

An event attribution is performed for the prolonged heat conditions over South Asia for March–April, 2022. This event struck India and Pakistan in March and April of 2022 and had a devastating impact on the socio-economic sector (Cappucci, 2022; Indian Council of Agricultural Research, 2022). The daily maximum temperatures occurring during this event were already shown to be made 30 times more likely due to climate change (Zachariah et al., 2023). However, providing attribution results for the persistent heat with explicitly represented natural climate variability would strengthen existing attribution results. The adapted MESMER framework is applied to both observational and ESM data. Given that MESMER can reproduce properties of an initial-condition ESM ensemble after training on only a single realisation of data (Beusch et al., 2020), the fidelity of natural climate variability representation is expected to hold for training on observations, ESMs with only a single initial-condition ensemble member, and ESMs with more than one initial-condition ensemble member. We investigate two approaches in which natural climate variability can be represented for event attribution: (1) where natural climate variability is represented as a single component; and (2) where the annual and seasonal components of natural climate variability are disentangled and represented separately. Event attribution results are calculated for both these modes separately, and compared to one another as well as to those obtained by the WWA approach.

The event to be attributed is defined as the mean temperature anomaly over the months of March and April, averaged over a homogeneous region covering the north-western parts of India and southeastern Pakistan, which witnessed the highest impacts during the persistent heat (see Fig. A.7). This is similar to the region and heatwave metric – March–April mean daily maximum temperature – used by Zachariah et al. (2023). The temperature anomalies are calculated with respect to the annual climatological mean over the reference period of 1950–1980.

The structure of this paper is as follows: Section 2 details the statistical methods used for attribution within this study, as divided into the WWA and this study's approach; Section 3 introduces the observational and ESM data used for attribution; Section 4 elaborates on the procedure used for evaluation; Section 5 provides the evaluation and final attribution results; and finally Section 6 proceeds to discussion and conclusions.

2. Statistical methods

For event attribution, we assess the increased likelihood of the event under the current factual climate compared to its likelihood to a hypothetical climate without anthropogenic influence. In this study we use Global Mean Surface Temperature (GMST) as a proxy of anthropogenic GHG forcings (i.e. as in Philip et al., 2020). The changing likelihood, referred to as the probability ratio, is estimated as the ratio between the event's likelihood at current GMST levels and a 1.2 °C cooler world (i.e. the temperature difference between current and pre-undustrial warming levels), referred to as past GMST levels. We furthermore assess how much cooler an event of the same likelihood would be at past GMST levels, referred to as the change in intensity.

In the following subsections, we detail the approaches used to construct the temperature distributions for the event, from which the probability ratio and change in intensity are obtained. We start by introducing the standard WWA approach, which is used as a reference point (Philip et al., 2020). We then introduce this study's methodology, which adapts the framework of the ESM emulator, MESMER, to provide a more explicit representation of natural climate variability.

2.1. World Weather Attribution (WWA) approach

WWA performs probabilistic event attribution, which entails modelling the likelihood of an event, conditional on anthropogenic GHG forcings (Philip et al., 2020; Zachariah et al., 2023). Smoothed GMSTs are used as a proxy of anthropogenic GHG forcings, and represent the mean global response to anthropogenic GHG emissions without the influence of natural climate variability. The conditional distribution of the event is modelled by means of a parameterised distribution (e.g., a normal or Generalised Extreme Value distribution) using smoothed GMST as a covariate. Since this study examines mean March–April temperatures averaged over the (large) study region, which can be assumed as normally distributed, we model it with a parameterised Gaussian distribution,

$$X \sim N(\mu(GMST), \sigma) \tag{1}$$

where $\mu(GMST)$ is modelled as a linear function of GMST,

$$\mu(GMST) = \beta_0 + \beta_1 \cdot GMST \tag{2}$$

and σ is constant over all GMST levels.

The parameterised Gaussian distribution is fit on observational data and for each ESM separately. All available members within an ESM initial-condition ensemble are pooled to fit the parameters. For observations and ESMs with only one initial-condition ensemble member, annual mean GMSTs are smoothed using a 4-year backwards running mean as done in the standard WWA approach (Philip et al., 2020). Otherwise, smoothed GMST trajectories are obtained as the average across all ESM initial-condition ensemble members. The main source of uncertainty considered in WWA is the parametric uncertainty, which we assess via sampling 1000 times using an MCMC sampler (Hauser et al., 2017). The standard WWA approach estimates the parametric uncertainty through bootstrapping, but MCMC sampling has already been used in several WWA studies (e.g., Ciavarella et al. (2021), Philip et al. (2022) and Zachariah et al. (2023)) and yields similar results.

It should be noted that by sampling several values of σ, the WWA method captures the uncertainty due to natural variability summed into that due to parametric uncertainty. Furthermore, since a single σ term is calculated, natural variability is assumed to be stationary with evolving GMST, and by calculating σ for a regionally averaged term, finer-scale spatially resolved processes underlying natural climate variability are unaccounted for.

2.2. Overview on this study's approach

This study seeks to explicitly treat natural climate variability for probabilistic event attribution. In comparison to the WWA method, this entails a more explicit representation of σ based on the stochastic, generative principles underlying ESM emulators, such that the uncertainty surrounding σ is also explicitly represented. We consider σ to be the natural climate variability surrounding the event, composed of short-term auto regressive and spatially correlated processes. We also incorporate a yearly-temperature dependent skewness into the monthly variability by use of the Yeo-Johnson power transformer present in MESMER-M's framework (Nath et al., 2022).

While σ could be empirically derived from a large ESM initial-condition ensemble, for the sake of attribution, we seek a method of representation that is applicable to observations, ESMs with a single realisation, and ESM initial-condition ensembles. This also allows for a more balanced comparison of the attribution results obtained between observations and ESMs. We thus adapt the framework of the ESM emulator MESMER, which specialises in representing natural climate variability. It does so by deterministically representing the long-term forced response of local yearly/monthly temperatures and stochastically modelling the residuals – which constitute natural climate variability – by means of a local AR(1) process with spatially correlated innovations (Beusch et al., 2020; Nath et al., 2022).

MESMER is first calibrated on ESM data to find the ESM-specific calibration parameters. Once calibrated on an ESM, MESMER can then generate spatially resolved fields of temperature emulations that approximate the distributional properties of that ESM's initial condition ensemble at any GMST level. We refer to Beusch et al. (2020) for further information on the calibration procedure for MESMER. Two approaches of adapting MESMER's framework are considered. The first treats natural climate variability as a single component to be sampled, and the second differentiates natural climate variability into its annual and seasonal components, to be sampled separately. In the following sections we outline the approach used by these two modes for event attribution.

2.2.1. Representing natural climate variability as a single component

To model the likelihood of the event conditional on GMSTs, we adapt MESMER's framework to represent mean March–April temperature anomalies $T_{s,y}^{MA}$ at a grid cell-level s and year y as follows,

$$T_{s,y}^{MA} = g_s(GMST_y^{trend}, GMST_y^{var}) + \eta_{s,y}^{MA} \qquad (3)$$

where g_s is a multivariate linear regression on $GMST_y^{trend}$ and $GMST_y^{var}$, which are the annual GMSTs smoothed using LOcally WEighted Scatterplot Smoothing (LOWESS) and their residuals, respectively. The variability term $\eta_{s,y}^{MA}$ represents the grid cell level residual variability surrounding $g_s(GMST_y^{trend}, GMST_y^{var})$ and is stochastically modelled by means of a grid cell specific AR(1) process with spatially correlated noise terms,

$$\eta_{s,y}^{MA} = \Gamma_s^{-1}(\gamma_{0,s} + \gamma_{1,s} \cdot \eta_{s,y-1}^{MA} + \sim N(0, \Sigma(r))) \qquad (4)$$

where Γ_s^{-1} is a grid cell specific inverse Yeo-Johnson power transformer to account for skewness in residual variabilities (Nath et al., 2022); γ_0 and γ_1 are the grid cell specific lag-1 autocorrelation coefficients; and $\Sigma(r)$ is a covariance matrix constructed across the residual variabilities of all grid cells. Since spatial correlations are expected to vanish with increasing distance, Σ is localised by means of a Gaspari-Cohn function (Gaspari and Cohn, 1999) with radius r. A 10-year spin up period is used to initialise the AR(1) process above. The described model corresponds to the MESMER emulator as described in Beusch et al. (2020), with a Yeo-Johnson power added to the residual variability term. In addition, March–April mean temperature anomalies are modelled, instead of annual mean temperatures as typically done with MESMER.

We calibrate the model presented in Eq. (3) on observational and ESM data separately. To minimise computational costs, we only calibrate grid cells with significant spatial correlations to the study region, by performing an initial calibration of the Gaspari-Cohn localisation radius, r, to the study region using a leave-one-year-out cross validation process with a maximum likelihood cost function (Beusch et al., 2020). The r obtained by this initial calibration is then kept fixed for the remainder of the calibration and generation of emulation process. All ESM initial-condition ensemble members are used during calibration. The parametric uncertainty of MESMER is assessed by performing calibration on year-wise bootstrap sampled sets of the input data. All years available within the training data are sampled with replacement, and 100 bootstraps are performed.

Once MESMER is calibrated, we generate 1000 T_s^{MA} emulated time series for each bootstrap sample (i.e., a total of 100×1000 emulated time series). A 3-year window around the GMST level of interest (both for current and past levels) is then sampled from which, the area-weighted average over the study region is taken to obtain the empirical distributions of the event at the GMST level of interest. The year corresponding to the past GMST level is obtained by identifying the closest match of LOWESS-smoothened GMSTs and 1.2 °C subtracted from the respective GMST of 2022. From the empirical distribution the event probability is determined as the fraction of emulations exceeding the event threshold. For observational data, the event threshold of 4.45 °C is used, and for ESMs the event is chosen as the temperature anomaly corresponding to the event return period as seen in observations.

2.2.2. Representing natural climate variability divided into annual and seasonal components

In the second approach, we aim to disentangle natural climate variability into annual and seasonal components. We model annual natural climate variability as year-to-year autocorrelations and the general, annual spatial covariance structures. The seasonal natural climate variability is then modelled as month-to-month autocorrelations and month-specific spatial covariance structures. To represent these variability components, we start by adapting the framework of MESMER-M, the monthly downscaling module of MESMER (Nath et al., 2022), as illustrated in Fig. 1, and elaborated in this section.

MESMER-M represents the temperature anomalies for a given month m, $T_{m,s,y}$ as

$$T_{m,s,y} = h_s(T_{s,y}, m) + \eta_{m,s,y} \qquad (5)$$

where $h_s(T_{s,y}, m)$ is a grid cell specific harmonic model that captures long-term trends in the seasonal cycle as a function of the local annual mean temperature ($T_{s,y}$), and $\eta_{m,s,y}$ represents the monthly, grid cell specific residual variability surrounding $h_s(T_{s,y}, m)$. The variability term $\eta_{m,s,y}$ is stochastically modelled using an AR(1) process similar to eq (4), but with month specific parameters,

$$\eta_{m,s,y} = \Gamma_{m,s}^{-1}(\gamma_{0,m,s} + \gamma_{1,m,s} \cdot \eta_{m-1,s,y} + N(0, \Sigma_m(r))) \qquad (6)$$

Since $h_s(T_{s,y}, m)$ has $T_{s,y}$ as a covariate, $\eta_{m,s,y}$ contains no interannual variability and is solely composed of month-to-month autocorrelations and month-specific spatial covariance structures. To obtain the seasonal natural climate variability for March and April ($\eta_{s,y}^{MA,Seas.}$), we emulate the variability terms for all months across all analysis years, and then take the mean of the modelled temperature variabilities $\eta_{m,s,y}$ over March and April for each analysis years. A 10-year spin up period is again used when emulating the variability terms for all months.

Following this, we note that $T_{s,y}$ also scales linearly with GMST, with some surrounding year-to-year variability. The harmonic model $h_s(T_{s,y}, m)$ thus still contains the year-to-year variability as propagated from $T_{s,y}$ alongside the GMST forced trend. To decompose $h_s(T_{s,y}, m)$ into these two components, we adapt the framework of MESMER. The mean over March and April for $h_s(T_{s,y}, m)$ outputs is first taken, from
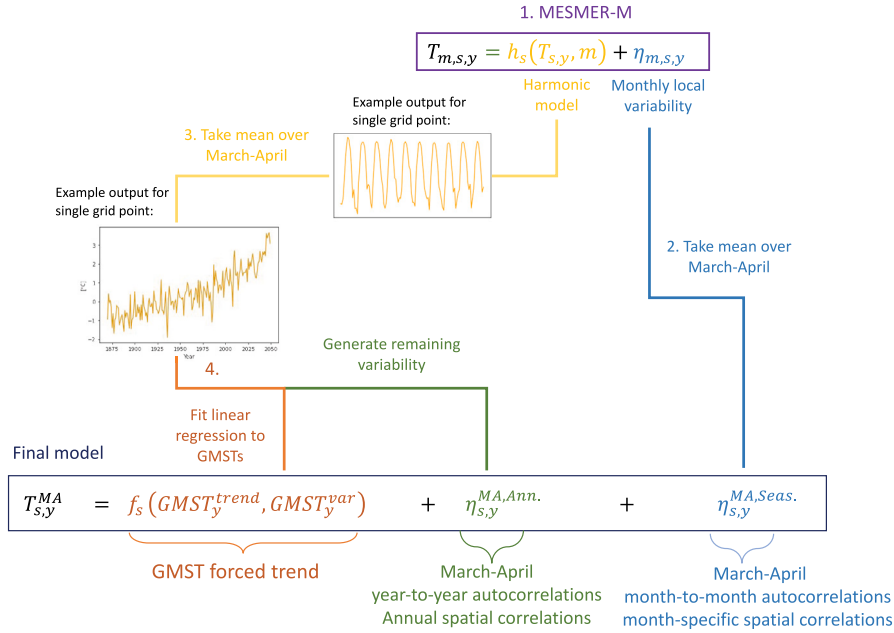
Fig. 1. Adaptation of MESMER-M framework for event attribution. From top to bottom: (1) MESMER-M, consisting of a harmonic model and a local monthly variability term, is calibrated. (2) The local monthly natural climate variability term, $\eta_{m,s,y}$, is used to calculate local, seasonal (i.e. March–April) natural climate variability ($\eta_{m,s}^{MA,Seas.}$). (3) Similarly, long-term forced March–April mean temperatures are calculated from the harmonic model of MESMER-M ($h_s(T_{s,y}, m)$). (4) These are then further decomposed into their forced responses to GMSTs and their surrounding variabilities as propagated from local, yearly temperature variabilities. The forced response to GMSTs is represented using a multivariate linear regression, $f_s(GMST_y^{trend}, GMST_y^{var})$, and the residuals representing the local, yearly variabilities are modelled as $\eta_{m,s}^{MA,Ann.}$.

which their GMST forced trend is derived using a multivariate linear regression similar to Eq. (3), $f_s(GMST_s^{trend}, GMST_s^{var})$. The residual variability surrounding $f_s(GMST_s^{trend}, GMST_s^{var})$ is considered to represent the year-to-year variability, $\eta_{s,y}^{MA,Ann.}$, and is stochastically modelled using an AR(1) process similar to Eq. (4) but without the Yeo-Johnson transformer,

$$\eta_{s,y}^{MA,Ann.} = \gamma_{0,s} + \gamma_{1,s} \cdot \eta_{s,y-1} + N(0, \Sigma(r)) \tag{7}$$

In such, we calibrate the adapted MESMER-M framework step by step for the month-to-month and year-to-year components of the natural climate variability surrounding $T_{s,y}^{MA}$, as well as their GMST forced responses to obtain the final model,

$$T_s^{MA} = f_s(GMST_y^{trend}, GMST_y^{var}) + \eta_{s,y}^{MA,Ann.} + \eta_{s,y}^{MA,Seas.} \tag{8}$$

The model in Eq. (8) is calibrated in a similar manner as that of Eq. (3). Again, 1000 T_s^{MA} values are sampled from a 3-year window around the GMST level of interest, for each bootstrap, and the area-weighted average over the study region taken, to then obtain the empirical distributions of the event. Finally, the event probability is determined as the fraction of emulations exceeding the event threshold.

We note that $\eta_{s,y}^{MA,Ann.}$ and $\eta_{s,y}^{MA,Seas.}$ are sampled independently from one another. This is a strong assumption that annual and seasonal variabilities can be represented separately. Ideally, $\eta_{s,y}^{MA,Ann.}$ and $\eta_{s,y}^{MA,Seas.}$ would be jointly sampled, however, for sake of simplicity and to stay within the scope of this study, we proceed with this approach.

3. Data

3.1. Observational data

We employ observational Berkeley Earth dataset (Rohde and Hausfather, 2020) of monthly surface temperature on a 1° x 1° gridded resolution. It provides comprehensive temporal coverage over the Indo-Pakistani region, starting from 1870, which is a century more than the ERA5 reanalysis product. For comparability with ESM data, Berkeley Earth data are regridded to a 2.5° by 2.5° grid using second-order conservative remapping, similar to the ESM data (Brunner et al., 2020).

3.2. CMIP6 data

Four ESMs from Phase 6 of the Coupled Model Intercomparison Project (CMIP6) (Eyring et al., 2016) are used in this study, namely AWI-CM-1-1-MR, CESM2-WACCM, IPSL-CM6A-LR and MPI-ESM1-2-LR. The ESMs are chosen as representative of different model genealogies (Knutti et al., 2013), and for their ability to represent the observational seasonal cycles (Zachariah et al., 2023) and atmospheric circulation features (Mahendra, 2021) of the region.

Historical simulations are employed until the year 2014, after which SSP5-8.5 simulations are used until the year 2050 (O'Neill et al., 2016). ESM simulations are obtained at a monthly resolution and are regridded to a common spatial resolution of 2.5° by 2.5° (Brunner et al., 2020). We note that, unlike observations with limited spatiotemporal coverage and especially until the mid-20th century, ESMs have comprehensive data coverage from 1850 onwards. Temperature values are expressed as anomalies with respect to the 1870–1900 annual climatological mean. Since attribution results are usually assessed relative to an ESM's distribution (van Oldenborgh et al., 2021), this should have no effect on the final results.

4. Evaluation

Both ESMs and Berkeley Earth data are evaluated across the analysis years available, i.e., 1870–2050 and 1870–2022 respectively. First, we evaluate the models in Eqs. (3) and (8), for their representation of the event's temperature distributions, by means of the Continuous Rank Probability Score (CRPS; Gneiting and Raftery, 2007). The CRPS provides a measure of the quadratic distance between the cumulative distribution function of the emulations at a given bootstrap ($T_{y,e}^{MA,i_{boot}}$) to that of the training data ($T_y^{MA,Tr.}$) as follows,

$$CRPS^{i_{boot}}(T_{y,e}^{MA,i_{boot}}, T_y^{MA,Tr.})_y =$$

$$\frac{1}{N_y} \Sigma_{y=1}^{y=N_y} [\int_{-\infty}^{+\infty} \frac{1}{N_e} \Sigma_{e=1}^{e=N_e} [\mathbb{1}_{(TMA \geq T_{y,e}^{MA,i_{boot}})} - \tag{9}$$

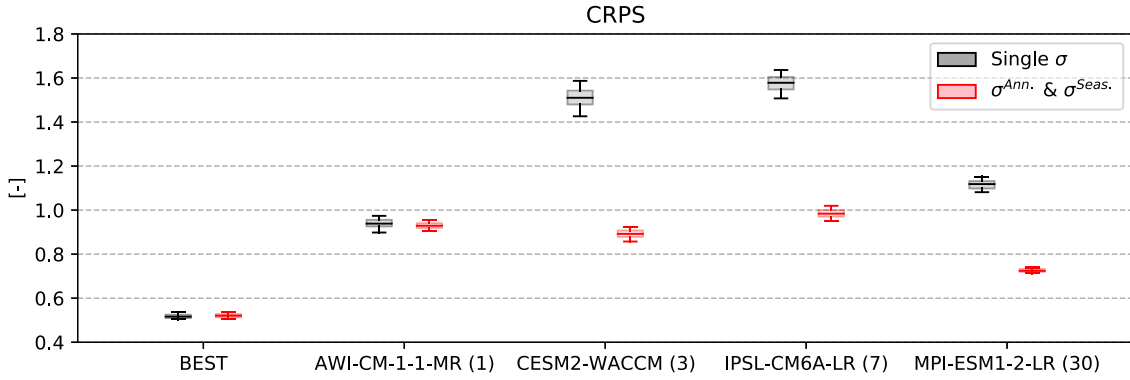$$\mathbb{1}_{(TMA \geq T_y^{MA,Tr.})}]^2 dT^{MA}]$$

Fig. 2. Continuous Rank Probability Scores (CRPS; smaller is better) obtained with the model treating natural climate variability as a single component, single σ (black), and the model treating the annual and seasonal components of natural climate variability separately, $\sigma^{Ann.}$ & $\sigma^{Seas.}$ (red). CRPS values are averaged over all timesteps for each bootstrap, and are shown for observational, Berkeley Earth data and ESMs. The number of available ESM training simulations are indicated in parentheses next to their names. Boxes indicate the interquartile range, and whiskers indicate the 90% confidence interval across all bootstraps. (For interpretation of the references to colour in this figure legend, the reader is referred to the web version of this article.)

The CRPS has been used within atmospheric sciences (Wilks, 2011; Jolliffe, 2012; Zamo and Naveau, 2018), as well as in the context of emulator evaluation (Quilcaille et al., 2022). The CRPS is calculated for each bootstrap, and is averaged over all available timesteps within the training data (N_y).

In addition, we seek to compare the uncertainties surrounding σ as obtained by the WWA method and Eqs. (3) and (8). For a consistent comparison, we first normalise their uncertainties to those present within the baseline climate system as represented by GMST. The natural climate variability of GMSTs, σ^{GMST} is rudimentarily obtained as the standard deviations over the $GMST^{var}$ term at each bootstrap (see Section 2.2.1). We define the ratio between the uncertainty (over the bootstrap samples) surrounding σ and σ^{GMST} as the Uncertainty Propagation Factor (UPF),

$$UPF = \frac{STDEV(\sigma)}{STDEV(\sigma^{GMST})}, \qquad (10)$$

where the standard deviations are calculated across all bootstraps for σ^{GMST} and for the σ values obtained using Eqs. (3) and (8), and across all MCMC samples for the σ values obtained using the WWA approach.

Such a ratio has been used in other fields — e.g., that of molecular dynamics, Vassaux et al. (2021) — to assess uncertainty propagation from the indicator variable (in our case GMST) to the variable of interest (i.e. the event), where a ratio below one indicates a dampening of uncertainty as propagated from GMSTs. For this study's application, we expect a UPF value of at least one, since the study region has more variability and is affected by faster processes (e.g. weather systems) in March–April than the entire globe at annual timescales, and hence GMST. Hence we expect no dampening of the uncertainties as propagated from σ^{GMST} to σ.

5. Results

In the following subsections, we first evaluate the three attribution methods (Section 2), and then compare the attribution results. The return period curves obtained by the methodologies introduced in this study are first visually compared to those obtained by the WWA methodology, followed by the final results for the event, expressed as probability ratios and changes in intensity.

5.1. Evaluation results

To evaluate the MESMER and MESMER-M based attribution, we first contrast CRPS of the two modes (Fig. 2). The mode treating natural climate variability as a single component (i.e., Eq. (3)) is referred to as "single σ", and the mode treating the annual and seasonal components of natural climate variability separately (i.e. Eq. (8)) is referred to as

"$\sigma^{Ann.}$ & $\sigma^{Seas.}$". Results are shown for both observational Berkeley Earth data and all ESMs. A higher CRPS value indicates poorer performance. There is generally little spread in CRPS results across all bootstraps. Both single σ and $\sigma^{Ann.}$ & $\sigma^{Seas.}$ perform better for Berkeley Earth than the ESMs, and this is likely caused by the fact that ESMs are evaluated for the training period of 1870–2050, while Berkeley Earth data is only evaluated for the training period of 1870–2022. Across all ESMs, $\sigma^{Ann.}$ & $\sigma^{Seas.}$ captures the temperature distributions for the event better than single σ. This shows that the added model complexity results in better accuracy in capturing the temperature distributions, indicating stronger monthly and yearly variability features (e.g. skewness and heteroskedasticity) displayed by ESMs, that cannot simply be deduced by scaling from GMSTs alone.

Fig. 3 shows boxplots of the UPF values across all bootstraps calculated at each timestep, obtained by single σ and $\sigma^{Ann.}$ & $\sigma^{Seas.}$ for Berkeley Earth and ESM data. UPF values calculated across all MCMC samples for WWA are provided as a reference, obtained as a single value for all timesteps. UPF values above (below) one indicate an amplification (dampening) in model uncertainty arising from natural climate variability as propagated from the indicator variable, GMST. Overall, single σ shows UPF values of at most two and are close to those of WWA, except for MPI-ESM1-2-LR. In contrast, $\sigma^{Ann.}$ & $\sigma^{Seas.}$ yields UPF values of at least two, which are generally higher than those of WWA and single σ. An increase in magnitude of UPF value and its spread across timesteps, with increase in number of ESM initial-condition ensemble members (as indicated in parentheses next to the ESM name) can be observed for $\sigma^{Ann.}$ & $\sigma^{Seas.}$. This results from a larger localisation radius favoured by the algorithm when there are more ESM initial-condition ensemble members available (see Table B.4), as also documented by Nath et al. (2022) during MESMER-M calibrations. Consequently, there is a larger amplification of uncertainty due to regional variability compared to what is propagated from GMST alone. Interestingly, the WWA approach reveals a decrease in magnitude of UPF values for an increasing number of initial-condition ensemble members. Furthermore, IPSL-CM6A-LR and MPI-ESM1-2-LR feature UPF values below one, indicating a dampening in uncertainty surrounding the event-level natural climate variability as propagated from GMSTs.

5.2. Attribution results

The observed mean temperature anomaly for the region over March and April 2022 is estimated as 4.45 °C using the Berkeley Earth Surface Temperature (Berkeley Earth) dataset (Rohde and Hausfather, 2020). Fig. 4 shows return period curves based on the WWA methodology, single σ and $\sigma^{Ann.}$ & $\sigma^{Seas.}$. Median return periods for the event at the current warming level are identified as 39, 27 and 46 years for WWA,
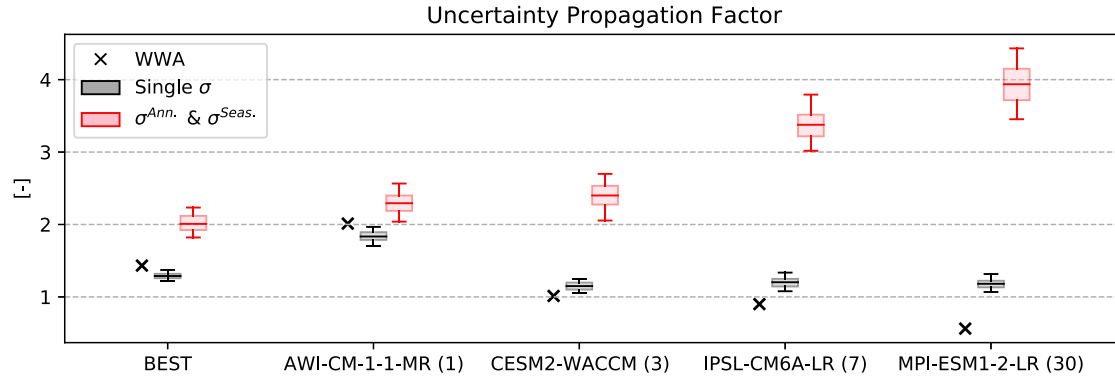
Fig. 3. Uncertainty Propagation Factors (UPF) obtained with the model treating natural climate variability as a single component, single σ (black), and the model treating the annual and seasonal components of natural climate variability separately, $\sigma^{Ann.}$ & $\sigma^{Seas.}$ (red). WWA results are provided as a reference (black cross). UPF values are calculated over all bootstraps (or MCMC samples for the WWA method), for each timestep, and are shown for observational, Berkeley Earth data and ESMs. The number of available ESM training simulations are indicated in parentheses next to their names. Boxes indicate the interquartile range, and whiskers indicate the 90% confidence interval across all timesteps. (For interpretation of the references to colour in this figure legend, the reader is referred to the web version of this article.)
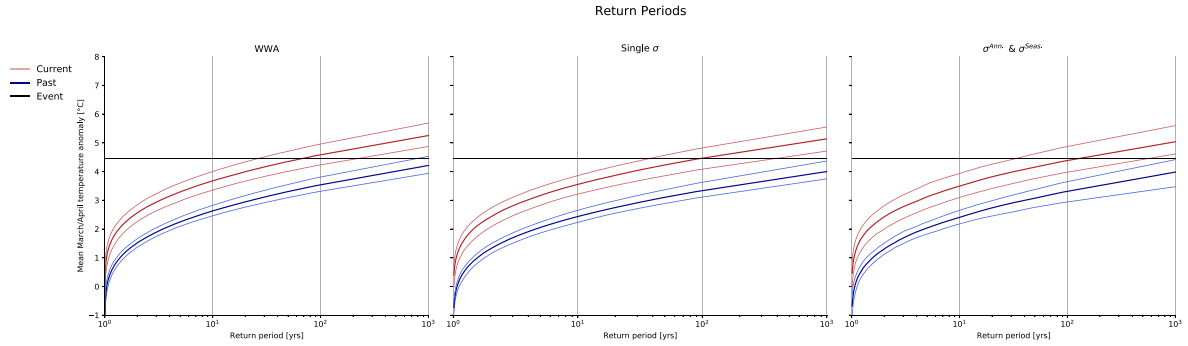

Fig. 4. Return period curves for Berkeley Earth data under past (blue) and current (red) warming levels. Curves obtained by the WWA methodology (left), single σ (middle) and $\sigma^{Ann.}$ & $\sigma^{Seas.}$ (right) are also shown. Dark lines indicate median values and light lines indicate the 90% confidence interval. (For interpretation of the references to colour in this figure legend, the reader is referred to the web version of this article.)

Table 1
Probability ratio [-], brackets indicate 90% confidence interval.

	WWA			Single σ			$\sigma^{Ann.}$ & σ^{Seas}		
	Curr.	1.5 °C	2 °C	Curr.	1.5 °C	2 °C	Curr.	1.5 °C	2 °C
Berkeley Earth	39 (10–141)	–	–	27 (2–225)	–	–	46 (2–985)	–	–
AWI-CM-1-1-MR (1)	1 (0–2)	1 (0–2)	1 (0–2)	1 (0–2)	1 (0–2)	1 (0–2)	3 (1–8)	4 (2–12)	7 (4–20)
CESM2-WACCM (3)	24 (15–37)	44 (26–74)	112 (60–203)	20 (13–48)	43 (26–75)	107 (57–230)	20 (6–60)	40 (15–121)	96 (28–296)
IPSL-CM6A-LR (7)	149 (100–207)	371 (236–540)	1278 (780–1949)	133 (81–301)	357 (208–738)	1263 (794–3075)	120 (29–799)	367 (96–2011)	1392 (380–6927)
MPI-ESM1-2-LR (30)	3 (2–4)	4 (3–5)	5 (4–6)	3 (2–4)	3 (2–5)	6 (4–9)	4 (1–13)	5 (2–19)	10 (4–37)
Multi-model average	44 (29–63)	105 (66–155)	349 (211–563)	39 (24–89)	101 (59–204)	344 (213–829)	36 (9–220)	104 (29–541)	377 (103–1820)
Synthesis	42 (20–102)	–	–	33 (13–157)	–	–	41 (6–603)	–	–

single σ and $\sigma^{Ann.}$ & $\sigma^{Seas.}$, respectively. The 95% confidence intervals in the current return period curves are similar between WWA and single σ, but wider for $\sigma^{Ann.}$ & $\sigma^{Seas.}$. This widening of the confidence interval is even more pronounced for the past return period curves. Fig. C.8 shows return period curves for all ESMs at past (−1.2 °C), current, 1.5 °C and 2 °C warming levels obtained by the WWA methodology, single σ and $\sigma^{Ann.}$ & $\sigma^{Seas.}$. There is a strong resemblance of the return period curves between all methodologies, again with larger uncertainty ranges for $\sigma^{Ann.}$ & $\sigma^{Seas.}$ that are more notable for past GMST levels. AWI-CM-1-1-MR is an exception to this, as it shows little change in return periods between different warming levels for WWA and single σ, while $\sigma^{Ann.}$ & $\sigma^{Seas.}$ display changes with increased GMST warming levels.

Figs. 5 and 6 provide boxplots of the probability ratio and change in intensity results, respectively, for the event obtained by WWA, single σ and $\sigma^{Ann.}$ & $\sigma^{Seas.}$. Results are shown for Berkeley Earth data (at current warming levels) and for all ESMs (at current, 1.5 °C and 2 °C warming

levels), values for the probability ratios and changes in intensity are also provided in Tables 1 and 2 respectively. Boxplots for single σ are overlaid on those for $\sigma^{Ann.}$ & $\sigma^{Seas.}$ to visualise the increase in uncertainty for a more complex model representation. Berkeley Earth data and all ESMs except AWI-CM-1-1-MR show similar probability ratio and change in intensity values between WWA, single σ and $\sigma^{Ann.}$ & $\sigma^{Seas.}$.

WWA and single σ results for AWI-CM-1-1-MR show lower increases in likelihoods and intensifications of the event as compared to $\sigma^{Ann.}$ & $\sigma^{Seas.}$. An inspection of the coefficients obtained for the normal parameterised distribution (see Fig. C.9) fitted in the WWA methodology reveals low values for the slope coefficients and high values for the standard deviation of AWI-CM-1-1-MR, indicating a weaker climate change signal as compared to the noise due to natural climate variability. $\sigma^{Ann.}$ & $\sigma^{Seas.}$ attribution results for AWI-CM-1-1-MR could thus be different from those of WWA and single σ, as a two-step trend extraction is performed, which may isolate a larger signal. $\sigma^{Ann.}$
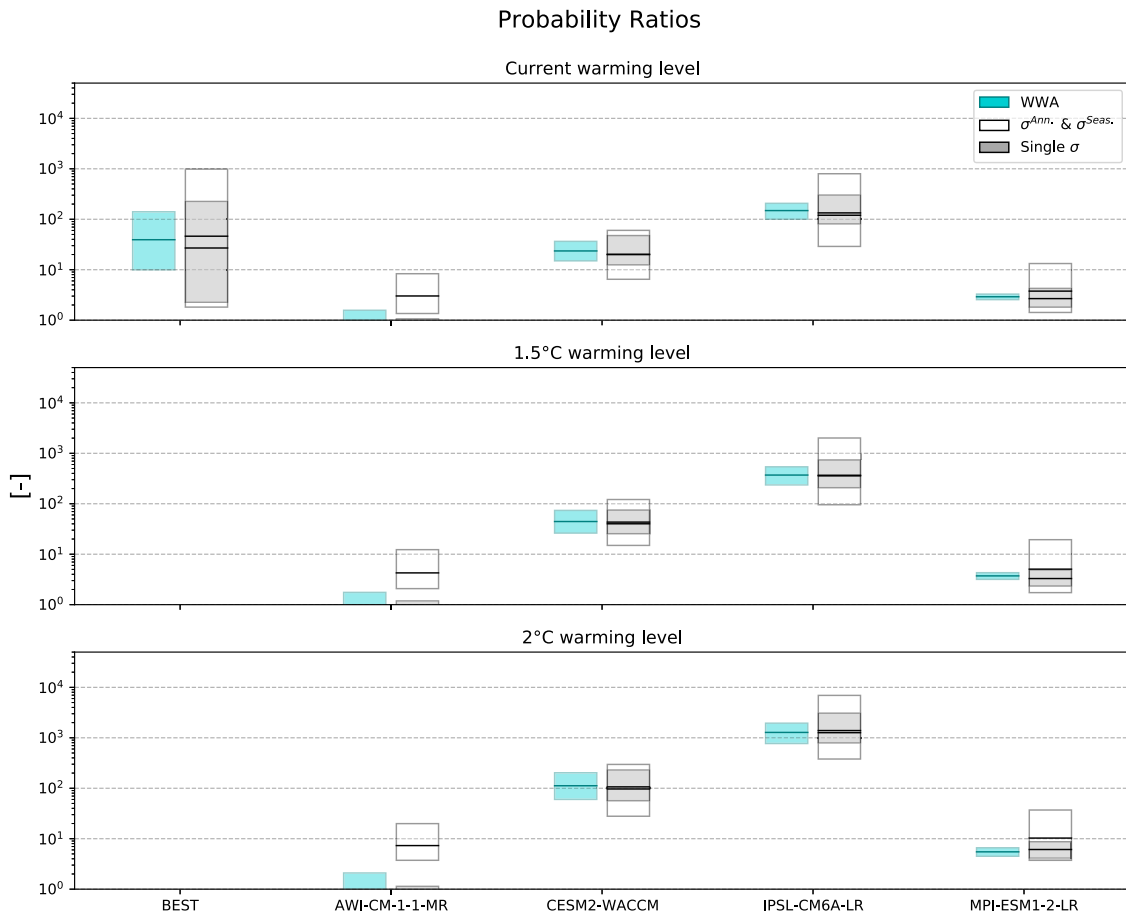
Probability Ratios

Fig. 5. Boxplots of probability ratios obtained by Berkeley Earth and for ESMs. WWA (blue), single σ (dark grey) and $\sigma^{Ann.}$ & $\sigma^{Seas.}$ (white) results are shown for current (top panel), 1.5 °C (middle panel), and 2 °C (bottom panel) warming levels. For Berkeley Earth data, results are only shown for current warming levels. Boxes indicate the 90% uncertainty level. Boxplots for single σ are overlaid on those for $\sigma^{Ann.}$ & $\sigma^{Seas.}$ to visualise the increase in uncertainty for more complex model representation. (For interpretation of the references to colour in this figure legend, the reader is referred to the web version of this article.)

Table 2
Change in intensity [°C], brackets indicate 90% confidence interval.

	WWA			Single σ			σ^{Ann} & σ^{Seas}		
	Curr.	1.5 °C	2 °C	Curr.	1.5 °C	2 °C	Curr.	1.5 °C	2 °C
Berkeley Earth	1.04 (0.67–1.38)	–	–	1.05 (0.68–1.52)	–	–	1.09 (0.30–1.63)	–	–
AWI-CM-1-1-MR (1)	−0.03 (−0.26–0.23)	−0.04 (−0.33–0.29)	−0.06 (−0.44–0.39)	−0.12 (−0.40–0.13)	−0.13 (−0.4–0.19)	−0.15 (−0.60–0.19)	0.45 (0.09–0.81)	0.60 (0.28–0.93)	0.78 (0.48–1.20)
CESM2-WACCM (3)	0.89 (0.79–0.99)	1.11 (0.99–1.24)	1.48 (1.32–1.65)	0.85 (0.73–1.03)	1.08 (0.94–1.24)	1.45 (1.25–1.62)	0.89 (0.61–1.23)	1.13 (0.84–1.44)	1.46 (1.07–1.76)
IPSL-CM6A-LR (7)	1.51 (1.43–1.56)	1.89 (1.79–1.95)	2.52 (2.38–2.60)	1.52 (1.35–1.69)	1.89 (1.74–2.07)	2.56 (2.32–2.75)	1.57 (1.21–1.88)	1.97 (1.57–2.29)	2.60 (2.22–3.04)
MPI-ESM1-2-LR (30)	0.43 (0.38–0.48)	0.54 (0.48–0.60)	0.72 (0.64–0.79)	0.40 (0.27–0.58)	0.48 (0.35–0.67)	0.74 (0.52–0.93)	0.50 (0.18–0.88)	0.65 (0.26–1.06)	0.89 (0.52–1.29))
Multi-model average	0.7 (0.59–0.82)	0.88 (0.73–1.02)	1.17 (0.98–1.36)	0.66 (0.48–0.83)	0.83 (0.66–1.05)	1.14 (0.86–1.37)	0.85 (0.52–1.20)	1.09 (0.74–1.43)	1.43 (1.07–1.82)
Synthesis	0.87 (0.63–1.1)	–	–	0.86 (0.58–1.16)	–	–	0.97 (0.41–1.42)	–	–

& $\sigma^{Seas.}$ results should thus be treated with caution as they may be overconfident in the extracted signal, especially when the surrounding noise due to natural climate variability is large.

Overall, probability ratio and change in intensity show considerably higher uncertainty bounds for $\sigma^{Ann.}$ & σ^{Seas} as compared to single σ and WWA. This is expected given the larger uncertainties in the return period curves obtained by $\sigma^{Ann.}$ & σ^{Seas}, particularly under past GMST levels. Given that the studied event falls in the tails of the temperature distributions for past GMST levels, a slight difference in the evaluated temperature distribution can lead to a huge impact on the obtained likelihood for the event, which will then significantly affect the increased likelihood and intensification results for the event under higher warming levels. Given that the uncertainty bounds are assessed by considering parametric uncertainty, this could originate from the added model complexity in $\sigma^{Ann.}$ & σ^{Seas}. However, it also highlights the uncertainties surrounding past temperature distributions that particularly arise from regional, annual and seasonal variabilities. Taking the ratio between 1.5 °C and current warming level multi-model

average results shows the event is 2.5 and 2.2 times more likely to occur for single σ and $\sigma^{Ann.}$ & σ^{Seas}, respectively. At 2 °C warming, the event has a 9 and 8.5-fold increase in likelihood as compared to current for single σ and $\sigma^{Ann.}$ & σ^{Seas}, respectively. WWA results show similar increases in likelihoods of the event under 1.5 and 2 °C warming levels as compared to current, i.e., 2.4 and 8 times increase, respectively. Moreover, the intensification of the event under 1.5 °C and 2 °C warming levels as compared to the current climate (i.e., when subtracting the change intensity of current warming levels from that of 1.5 °C/2 °C), correspond well between WWA, single σ and $\sigma^{Ann.}$ & σ^{Seas}, with values of 0.18–0.24 and 0.47–0.66 at each respective warming level. This provides strong consensus on the scaling of the increased likelihood and intensification of the event with increased global warming levels.

6. Discussion and conclusion

This study demonstrates the reproducibility of probabilistic extreme event attribution when explicitly treating natural climate variability.
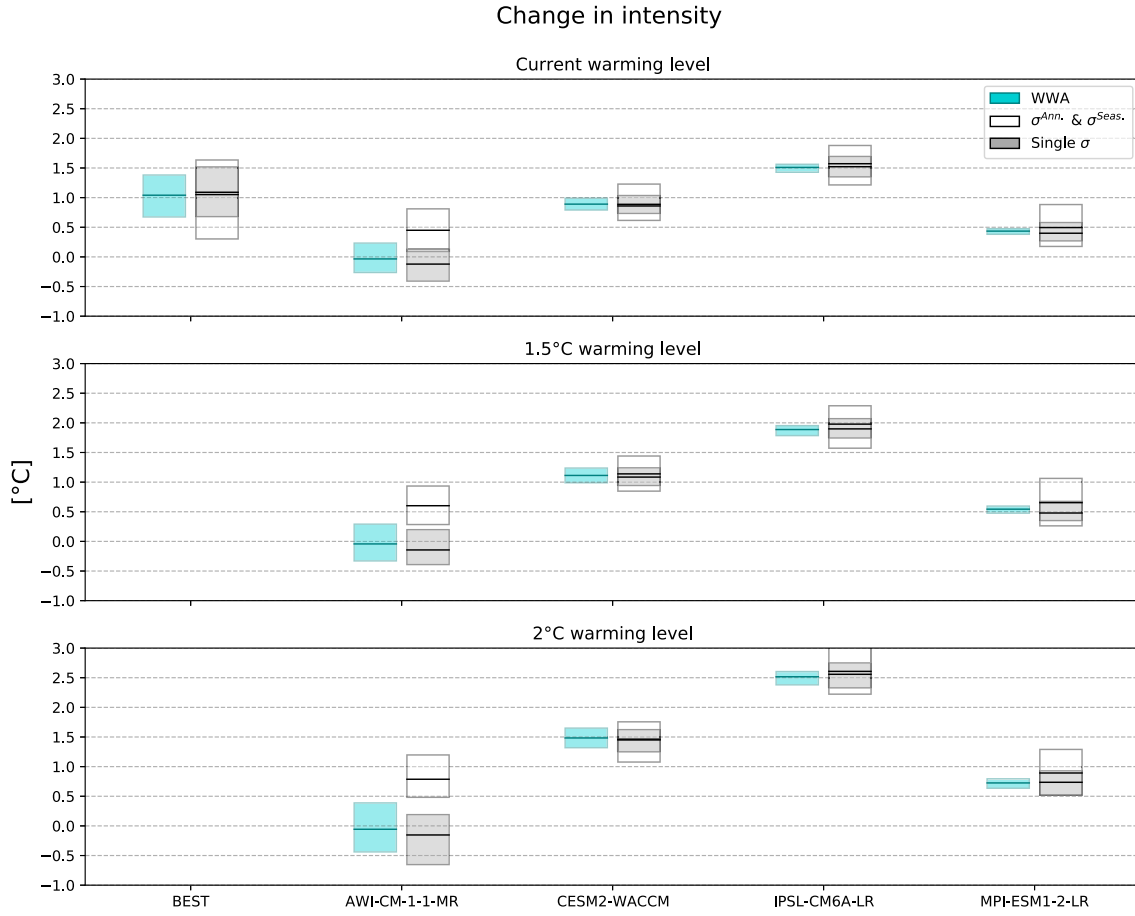
Change in intensity

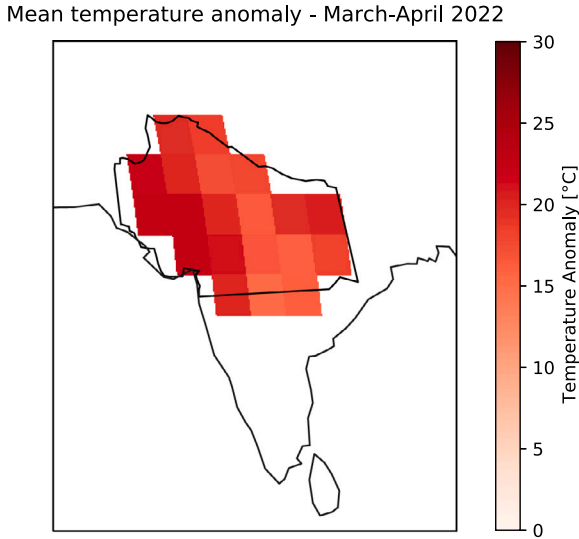**Fig. 6.** Same as Fig. 5 but for change in intensity.

Fig. A.7. Event definition: the region of interest and the average, absolute temperatures recorded over it during March/April 2022 by Berkeley Earth data is shown.

The methodology underlying the ESM emulator MESMER is used to represent natural climate variability, and results are compared to those obtained using the WWA approach. An event attribution is carried out on the prolonged March–April heat conditions of 2022 over India and Pakistan. For probabilistic extreme event attribution, we are mainly interested in constructing the temperature distributions for the studied event conditional on GMSTs, which are used as a proxy for anthropogenic GHG forcings. We assess natural climate variability as composed of grid cell-level short-term, spatially correlated patterns, and adapt MESMER's framework to model and generate these patterns alongside the grid cell level mean temperature responses to GMSTs. By sampling the generated temperature terms around a 3-year window of a given GMST level, we then obtain the desired temperature distributions for the studied event at that GMST level, such that the surrounding natural climate variability is explicitly represented. Two modes of adapting MESMER's framework to represent natural climate variability are explored: (1) where natural climate variability is treated as a single component (single σ); and (2) where natural climate variability is treated as separate annual and seasonal components ($\sigma^{Ann.}$ & $\sigma^{Seas.}$).

The adapted frameworks, single σ and $\sigma^{Ann.}$ & $\sigma^{Seas.}$, are calibrated on observational Berkeley Earth and ESM data from CMIP6. Calibration is performed on bootstrap-resampled sets of training data to also quantify the underlying parametric uncertainties. The resulting temperature distributions for the studied event are evaluated by means of the Continuous Rank Probability Score (CRPS). Generally, single σ shows poorer performance than $\sigma^{Ann.}$ & $\sigma^{Seas.}$, indicating that separately treating the annual and seasonal components of natural climate variability allows for better representation of the temperature distributions. Following this, we also test the model uncertainty surrounding natural climate variability as propagated from the indicator variable, GMST, by means of the Uncertainty Propagation Factor (UPF). UPFs obtained for the WWA approach are also provided as a reference. We observe that the added model complexity of $\sigma^{Ann.}$ & $\sigma^{Seas.}$ leads to higher model uncertainties as compared to single σ and WWA, and that this tends to be more pronounced for larger initial-condition ESM ensembles. There is no way to determine the 'right' level of UPF for
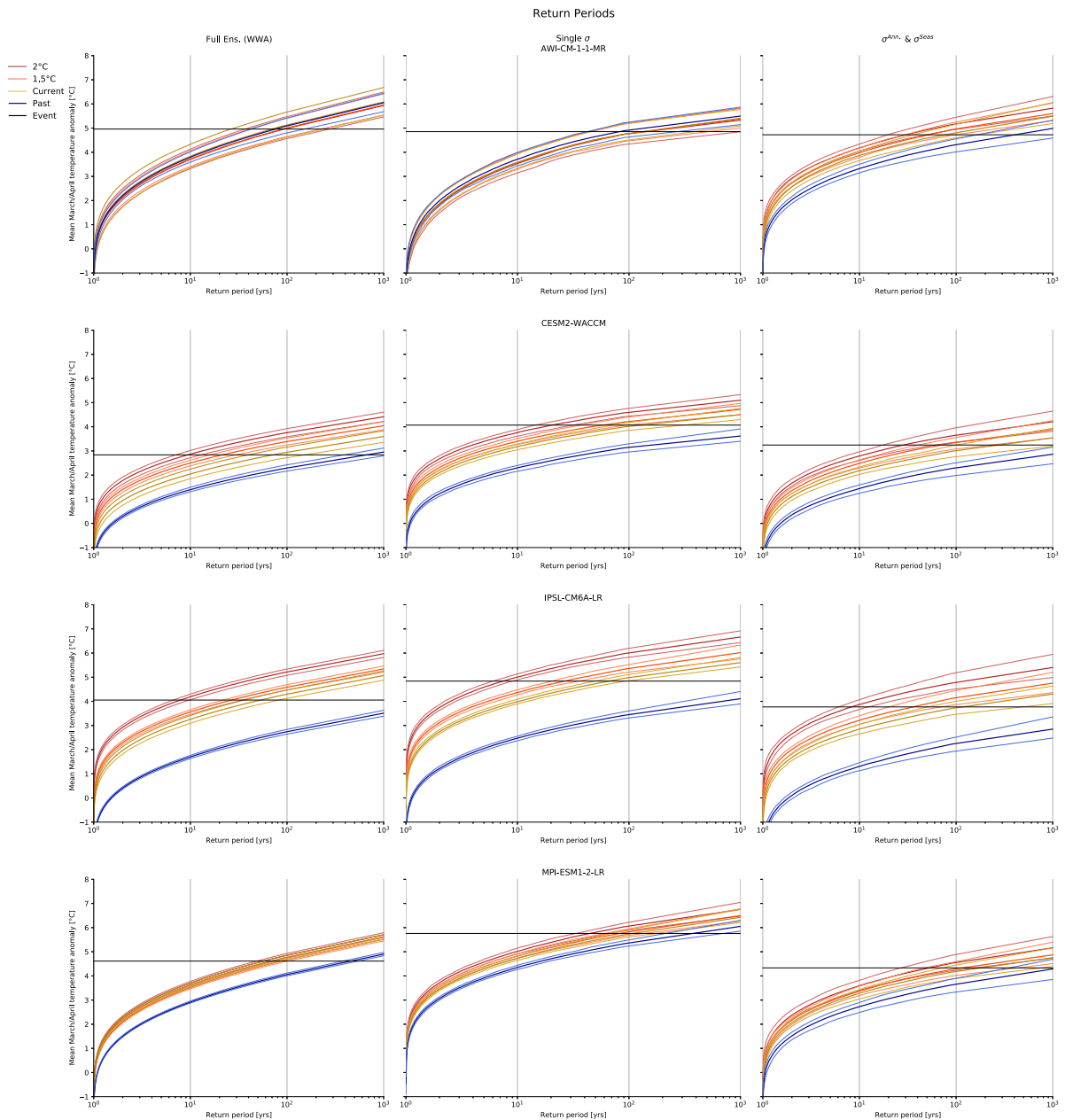
Fig. C.8. Return period curves for all ESMs under past (blue), current (yellow), 1.5 °C (orange) and 2 °C (red) warming levels. Curves obtained by the WWA methodology (left), single σ (middle) and $\sigma^{Ann.}$ & $\sigma^{Seas.}$ (right) are shown. (For interpretation of the references to colour in this figure legend, the reader is referred to the web version of this article.)

the different methods considered. What our results show, however, is that with increasing complexity of the statistical method, the UPF increases. The reasons for this can be principally two-fold: (1) An explicit representation of different modes of natural variability based on regional and seasonal spatio-temporal covariance structures highlights the importance of their underlying modes of variability. (2) Due to the increased model complexity, parameter uncertainty increases (also noting the potential over-estimation of uncertainty due to an assumed independence of annual and seasonal natural variability).

Probability ratio and change in intensity attribution results for the event are calculated using the empirical distributions obtained by single σ and $\sigma^{Ann.}$ & $\sigma^{Seas.}$, while WWA results are provided as a reference. Starting with the observational attribution results, single σ and $\sigma^{Ann.}$ & $\sigma^{Seas.}$ show similar median probability ratio and change in intensity values to those of WWA. The uncertainty ranges of $\sigma^{Ann.}$ & $\sigma^{Seas.}$

encompass and are much larger than those of single σ and WWA. ESM results show agreement in probability ratio and change in intensity values obtained by single σ, $\sigma^{Ann.}$ & $\sigma^{Seas.}$ and WWA except for AWI-CM-1-1-MR, where $\sigma^{Ann.}$ & $\sigma^{Seas.}$ shows markedly different results from single σ and WWA. We hypothesise that this difference arises from the two step signal extraction performed in $\sigma^{Ann.}$ & $\sigma^{Seas.}$ which may result in overconfidence of the climate change signal.

Overall, synthesis results (i.e. multi-model average + observational) for WWA, single σ and $\sigma^{Ann.}$ & $\sigma^{Seas.}$ indicate the event being made 42, 33 and 41 times more likely, respectively, due to GMST increase since pre-industrial times. This corresponds to a 0.87, 0.86 and 0.97 °C hotter event as compared to an event of the same return period under a 1.2 °C cooler world obtained by WWA, single σ and $\sigma^{Ann.}$ & $\sigma^{Seas.}$, respectively. Between all methodologies, multi-model average results indicate approximately a 10-fold increase in likelihood, and a 1 °C
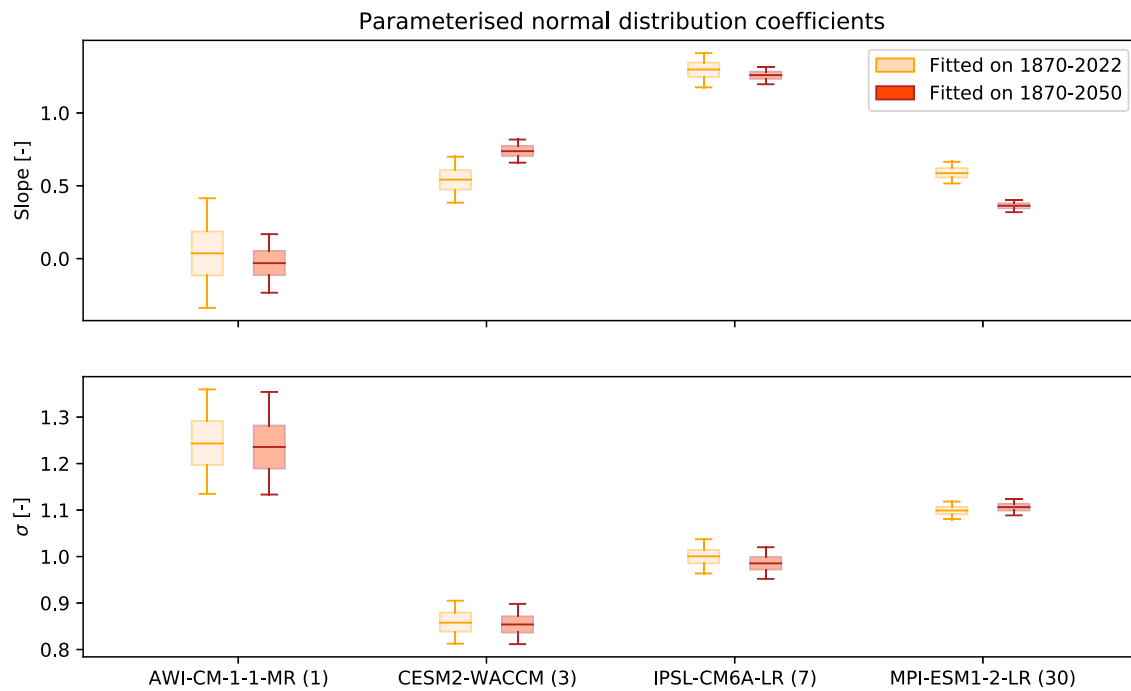
Fig. C.9. Coefficients obtained for the normal parameterised distribution fitted on ESMs in the WWA approach. Distributions were fitted over two different time periods: 1870–2022 (orange) used to obtain current attribution results; 1870–2050 (red) used to obtain higher warming level attribution results. (For interpretation of the references to colour in this figure legend, the reader is referred to the web version of this article.)

intensification of the event for every additional 1 °C increase in GMST levels. Thus, by employing various probabilistic extreme event attribution approaches, with a particular focus into representing uncertainty in the contributions of natural climate variability, we demonstrate clear consensus in the final attribution results: any additional global warming increases the frequency and intensity of persistent heat extremes with large spatial extent as well as societal impacts, such as the India-Pakistani 2022 heatwave.

Code and data availability

MESMER and MESMER-M are publicly available under Github (Hauser et al., 2021; Nath, 2022). The CMIP6 data are available from the public CMIP archive at https://esgf-node.llnl.gov/projects/esgf-llnl/, and Berkeley Earth data are publicly available from https://berkeleyearth.org/data/

CRediT authorship contribution statement

Shruti Nath: Writing – original draft, Software, Methodology, Formal analysis, Conceptualization. **Mathias Hauser:** Writing – review & editing, Validation, Methodology, Formal analysis. **Dominik L. Schumacher:** Writing – review & editing, Validation, Methodology, Formal analysis. **Quentin Lejeune:** Writing – review & editing, Supervision, Conceptualization. **Lukas Gudmundsson:** Writing – review & editing. **Yann Quilcaille:** Writing – review & editing. **Pierre Candela:** Validation, Methodology, Formal analysis. **Fahad Saeed:** Writing – review & editing. **Sonia I. Seneviratne:** Writing – review & editing, Supervision. **Carl-Friedrich Schleussner:** Writing – review & editing, Supervision, Conceptualization.

Declaration of competing interest

The authors declare that they have no known competing financial interests or personal relationships that could have appeared to influence the work reported in this paper.

Data availability

MESMER and MESMER-M are publicly available under Github (Hauser et al., 2021; Nath, 2022). The CMIP6 data are available from the public CMIP archive at https://esgf-node.llnl.gov/projects/esgf-llnl/, and Berkeley Earth data are publicly available from https://berkeleyearth.org/data/.

Appendix A

See Fig. A.7.

Appendix B

See Tables B.3 and B.4.

Appendix C

See Figs. C.8 and C.9.

Table B.3

List of the 4 employed CMIP6 models, the modelling groups providing them, and their number of initial-condition ensemble members.

Model	Modelling centre (or group)	Ensemble members
AWI-CM-1-1-MR	Alfred Wegener Institute, Helmholtz Centre for Polar and Marine Research	1
CESM2-WACCM	National Center for Atmospheric Research	3
IPSL-CM6A-LR	Institut Pierre-Simon Laplace	7
MPI-ESM1-2-LR	Max–Planck-Institut für Meteorologie (Max Planck Institute for Meteorology)	30

Table B.4

Localisation radii selected for Berkeley Earth and ESM data.

	Localisation radius [m]
Berkeley Earth	2750
AWI-CM-1-1-MR	2750
CESM2-WACCM	3500
IPSL-CM6A-LR	5500
MPI-ESM1-2-LR	5750

References

Beusch, L., Gudmundsson, L., Seneviratne, S.I., 2020. Emulating Earth system model temperatures with MESMER: from global mean temperature trajectories to grid-point-level realizations on land. Earth Syst. Dyn. 11 (1), 139–159. http://dx.doi.org/10.5194/esd-11-139-2020, URL: https://esd.copernicus.org/articles/11/139/2020/.

Beusch, L., Nauels, A., Gudmundsson, L., Gütschow, J., Schleussner, C.-F., Seneviratne, S.I., 2022. Responsibility of major emitters for country-level warming and extreme hot years. Commun. Earth Environ. 3 (1), 7. http://dx.doi.org/10.1038/s43247-021-00320-6.

Brunner, L., Pendergrass, A.G., Lehner, F., Merrifield, A.L., Lorenz, R., Knutti, R., 2020. Reduced global warming from CMIP6 projections when weighting models by performance and independence. Earth Syst. Dyn. 11 (4), 995–1012. http://dx.doi.org/10.5194/esd-11-995-2020, URL: https://esd.copernicus.org/articles/11/995/2020/.

Cappucci, M., 2022. Record heat has gripped India since March. It's about to get worse. URL: https://www.washingtonpost.com/weather/2022/04/25/india-record-heat-march-april/.

Ciavarella, A., Cotterill, D., Stott, P., Kew, S., Philip, S., van Oldenborgh, G.J., Skålevåg, A., Lorenz, P., Robin, Y., Otto, F., Hauser, M., Seneviratne, S.I., Lehner, F., Zolina, O., 2021. Prolonged Siberian heat of 2020 almost impossible without human influence. Clim. Change 166 (1–2), 9. http://dx.doi.org/10.1007/s10584-021-03052-w, URL: https://link.springer.com/10.1007/s10584-021-03052-w.

Eyring, V., Bony, S., Meehl, G.A., Senior, C.A., Stevens, B., Stouffer, R.J., Taylor, K.E., 2016. Overview of the Coupled Model Intercomparison Project Phase 6 (CMIP6) experimental design and organization. Geosci. Model Dev. 9 (5), 1937–1958. http://dx.doi.org/10.5194/gmd-9-1937-2016.

Gaspari, G., Cohn, S.E., 1999. Construction of correlation functions in two and three dimensions. Q. J. R. Meteorol. Soc. 125 (554), 723–757. http://dx.doi.org/10.1256/smsqj.55416.

Gneiting, T., Raftery, A.E., 2007. Strictly proper scoring rules, prediction, and estimation. J. Amer. Statist. Assoc. 102 (477), 359–378. http://dx.doi.org/10.1198/016214506000001437, URL: http://www.tandfonline.com/doi/abs/10.1198/016214506000001437.

Hauser, M., Beusch, L., Nicholls, Z., Schwaab, J., 2021. MESMER-group/mesmer: version 0.8.3. http://dx.doi.org/10.5281/zenodo.5802054.

Hauser, M., Gudmundsson, L., Orth, R., Jézéquel, A., Haustein, K., Vautard, R., van Oldenborgh, G.J., Wilcox, L., Seneviratne, S.I., 2017. Methods and model dependency of extreme event attribution: The 2015 European drought. Earth's Future 5 (10), 1034–1043. http://dx.doi.org/10.1002/2017EF000612, URL: http://doi.wiley.com/10.1002/2017EF000612.

Indian Council of Agricultural Research, 2022. Heat wave 2022: causes, impacts and way forward for Indian agriculture. URL: http://www.indiaenvironmentportal.org.in/content/473323/heat-wave-2022-causes-impacts-and-way-forward-for-indian-agriculture/.

Jolliffe, I., 2012. Forecast Verificaton: A Practitioner's Guide in Atmospheric Science, second ed. Wiley-Blackwell, Oxford.

Kimutai, J., New, M., Wolski, P., Otto, F., 2022. Attribution of the human influence on heavy rainfall associated with flooding events during the 2012, 2016, and 2018 March-April-May seasons in Kenya. Weather Clim. Extrem. 38, 100529. http://dx.doi.org/10.1016/j.wace.2022.100529, URL: https://linkinghub.elsevier.com/retrieve/pii/S2212094722001086.

Knutti, R., Masson, D., Gettelman, A., 2013. Climate model genealogy: Generation CMIP5 and how we got there. Geophys. Res. Lett. 40 (6), 1194–1199. http://dx.doi.org/10.1002/grl.50256.

Mahendra, N., 2021. Interdecadal modulation of interannual ENSO-Indian summer monsoon rainfall teleconnections in observations and CMIP6 models : Regional patterns. pp. 2528–2552. http://dx.doi.org/10.1002/joc.6973.

Meinshausen, M., Wigley, T.M., Raper, S.C., 2011. Emulating atmosphere-ocean and carbon cycle models with a simpler model, MAGICC6 - Part 2: Applications. Atmos. Chem. Phys. 11 (4), 1457–1471. http://dx.doi.org/10.5194/acp-11-1457-2011.

Nath, S., 2022. snath-xoc/Nath_et_al_ESD_2022_MESMER-M. http://dx.doi.org/10.5281/ZENODO.6477494, URL: https://zenodo.org/record/6477494.

Nath, S., Lejeune, Q., Beusch, L., Seneviratne, S.I., Schleussner, C.F., 2022. MESMER-M: an Earth system model emulator for spatially resolved monthly temperature. Earth Syst. Dyn. 13 (2), 851–877. http://dx.doi.org/10.5194/esd-13-851-2022.

van Oldenborgh, G.J., van der Wiel, K., Kew, S., Philip, S., Otto, F., Vautard, R., King, A., Lott, F., Arrighi, J., Singh, R., van Aalst, M., 2021. Pathways and pitfalls in extreme event attribution. Clim. Change 166 (1–2), 1–27. http://dx.doi.org/10.1007/s10584-021-03071-7.

O'Neill, B.C., Tebaldi, C., Van Vuuren, D.P., Eyring, V., Friedlingstein, P., Hurtt, G., Knutti, R., Kriegler, E., Lamarque, J.F., Lowe, J., Meehl, G.A., Moss, R., Riahi, K., Sanderson, B.M., 2016. The scenario model intercomparison project (ScenarioMIP) for CMIP6. Geosci. Model Dev. 9 (9), 3461–3482. http://dx.doi.org/10.5194/gmd-9-3461-2016.

Otto, F.E., Boyd, E., Jones, R.G., Cornforth, R.J., James, R., Parker, H.R., Allen, M.R., 2015. Attribution of extreme weather events in Africa: a preliminary exploration of the science and policy implications. Clim. Change 132 (4), 531–543. http://dx.doi.org/10.1007/s10584-015-1432-0.

Otto, F.E.L., Massey, N., Oldenborgh, G.J.V., Jones, R.G., Allen, M.R., 2012. Reconciling two approaches to attribution of the 2010 Russian heat wave. pp. 1–5. http://dx.doi.org/10.1029/2011GL050422, 39.

Philip, S.Y., Kew, S.F., van Oldenborgh, G.J., Anslow, F.S., Seneviratne, S.I., Vautard, R., Coumou, D., Ebi, K.L., Arrighi, J., Singh, R., van Aalst, M., Pereira Marghidan, C., Wehner, M., Yang, W., Li, S., Schumacher, D.L., Hauser, M., Bonnet, R., Luu, L.N., Lehner, F., Gillett, N., Tradowsky, J.S., Vecchi, G.A., Rodell, C., Stull, R.B., Howard, R., Otto, F.E.L., 2022. Rapid attribution analysis of the extraordinary heat wave on the Pacific coast of the US and Canada in June 2021. Earth Syst. Dyn. 13 (4), 1689–1713. http://dx.doi.org/10.5194/esd-13-1689-2022, URL: https://esd.copernicus.org/articles/13/1689/2022/.

Philip, S., Kew, S., van Oldenborgh, G.J., Otto, F., Vautard, R., van der Wiel, K., King, A., Lott, F., Arrighi, J., Singh, R., van Aalst, M., 2020. A protocol for probabilistic extreme event attribution analyses. Adv. Stat. Climatol. Meteorol. Oceanogr. 6 (2), 177–203. http://dx.doi.org/10.5194/ascmo-6-177-2020.

Philip, S.Y., Kew, S.F., Oldenborgh, G.J.V., Yang, W., Vecchi, G.A., Anslow, F.S., Li, S., Seneviratne, S.I., Luu, L.N., Arrighi, J., Singh, R., Aalst, V., Hauser, M., Schumacher, D.L., Marghidan, C.P., Ebi, K.L., Vautard, R., Tradowsky, J., Coumou, D., Lehner, F., Rodell, C., Stull, R., Howard, R., Gillett, N., Otto, F.E.L., 2021. Rapid attribution analysis of the extraordinary heatwave on the Pacific Coast of the US and Canada June 2021. World Weather Attrib. (June), 119–123, URL: https://www.worldweatherattribution.org/wp-content/uploads/NW-US-extreme-heat-2021-scientific-report-WWA.pdf.

Quilcaille, Y., Gudmundsson, L., Beusch, L., Hauser, M., Seneviratne, S.I., 2022. Showcasing MESMER-X: Spatially resolved emulation of annual maximum temperatures of earth system models. Geophys. Res. Lett. 49 (17), 1–11. http://dx.doi.org/10.1029/2022GL099012, URL: http://www.essoar.org/doi/10.1002/essoar.10511207.1 https://onlinelibrary.wiley.com/doi/10.1029/2022GL099012.

Rohde, R.A., Hausfather, Z., 2020. The Berkeley Earth land/ocean temperature record. Earth Syst. Sci. Data 12 (4), 3469–3479. http://dx.doi.org/10.5194/essd-12-3469-2020.

Smith, C.J., Forster, P.M., Allen, M., Leach, N., Millar, R.J., Passerello, G.A., Regayre, L.A., 2017. FAIR v1.1: A simple emissions-based impulse response and carbon cycle model. Geosci. Model Dev. Discuss. (December), 1–45. http://dx.doi.org/10.5194/gmd-2017-266.

Stott, P.A., Christidis, N., Otto, F.E.L., Sun, Y., Vanderlinden, J.-P., van Oldenborgh, G.J., Vautard, R., von Storch, H., Walton, P., Yiou, P., Zwiers, F.W., 2016. Attribution of extreme weather and climate-related events. WIREs Clim. Change 7 (1), 23–41. http://dx.doi.org/10.1002/wcc.380, URL: https://onlinelibrary.wiley.com/doi/10.1002/wcc.380.

Tebaldi, C., Arblaster, J.M., 2014. Pattern scaling: Its strengths and limitations, and an update on the latest model simulations. Clim. Change 122 (3), 459–471. http://dx.doi.org/10.1007/s10584-013-1032-9.

Van Oldenborgh, G.J., Philip, S., Kew, S., Van Weele, M., Uhe, P., Otto, F., Singh, R., Pai, I., Cullen, H., Achutarao, K., 2018. Extreme heat in India and anthropogenic climate change. Nat. Hazards Earth Syst. Sci. 18 (1), 365–381. http://dx.doi.org/10.5194/nhess-18-365-2018.

Vassaux, M., Wan, S., Edeling, W., Coveney, P.V., 2021. Ensembles are required to handle aleatoric and parametric uncertainty in molecular dynamics simulation. J. Chem. Theory Comput. 17 (8), 5187–5197. http://dx.doi.org/10.1021/acs.jctc.1c00526, URL: https://pubs.acs.org/doi/10.1021/acs.jctc.1c00526.

Watson-parris, D., Smith, C.J., 2022. Large uncertainty in future warming due to aerosol forcing. http://dx.doi.org/10.1038/s41558-022-01516-0, 12.

Wilks, D.S., 2011. Statistical Methods in the Atmospheric Sciences, third ed. Academic Press.

Zachariah, M., Arulalan, T., AchutaRao, K., Saeed, F., Jha, R., Dhasmana, M.K., Mondal, A., Bonnet, R., Vautard, R., Philip, S., Kew, S., Vahlberg, M., Singh, R., Arrighi, J., Heinrich, D., Thalheimer, L., Marghidan, C.P., Kapoor, A., van Aalst, M., Raju, E., Li, S., Sun, J., Vecchi, G., Yang, W., Hauser, M., Schumacher, D.L., Seneviratne, S.I., Harrington, L.J., Otto, F.E.L., 2023. Attribution of 2022 early-spring heatwave in India and Pakistan to climate change: lessons in assessing vulnerability and preparedness in reducing impacts. Environ. Res.: Clim. 2 (4), 045005. http://dx.doi.org/10.1088/2752-5295/acf4b6, URL: https://www.worldweatherattribution.org/climate-change-made-devastating-early-heat-in-india-and-pakistan-30-times-more-likely/ https://iopscience.iop.org/article/10.1088/2752-5295/acf4b6.

Zamo, M., Naveau, P., 2018. Estimation of the continuous ranked probability score with limited information and applications to ensemble weather forecasts. Math. Geosci. 50 (2), 209–234. http://dx.doi.org/10.1007/s11004-017-9709-7, URL: http://link.springer.com/10.1007/s11004-017-9709-7.